

# Journal of Biomedical Optics

BiomedicalOptics.SPIEDigitalLibrary.org

## **Spectrally resolved fluorescence lifetime imaging to investigate cell metabolism in malignant and nonmalignant oral mucosa cells**

Angelika Rück  
Carmen Hauser  
Simone Mosch  
Sviatlana Kalinina

# Spectrally resolved fluorescence lifetime imaging to investigate cell metabolism in malignant and nonmalignant oral mucosa cells

Angelika Rück,\* Carmen Hauser, Simone Mosch, and Sviatlana Kalinina  
University Ulm, Core Facility Laser Microscopy, N24, Albert Einstein Allee 11, 89081 Ulm, Germany

**Abstract.** Fluorescence-guided diagnosis of tumor tissue is in many cases insufficient, because false positive results interfere with the outcome. Improvement through observation of cell metabolism might offer the solution, but needs a detailed understanding of the origin of autofluorescence. With respect to this, spectrally resolved multiphoton fluorescence lifetime imaging was investigated to analyze cell metabolism in metabolic phenotypes of malignant and nonmalignant oral mucosa cells. The time-resolved fluorescence characteristics of NADH were measured in cells of different origins. The fluorescence lifetime of bound and free NADH was calculated from biexponential fitting of the fluorescence intensity decay within different spectral regions. The mean lifetime was increased from nonmalignant oral mucosa cells to different squamous carcinoma cells, where the most aggressive cells showed the longest lifetime. In correlation with reports in the literature, the total amount of NADH seemed to be less for the carcinoma cells and the ratio of free/bound NADH was decreased from nonmalignant to squamous carcinoma cells. Moreover for squamous carcinoma cells a high concentration of bound NADH was found in cytoplasmic organelles (mainly mitochondria). This all together indicates that oxidative phosphorylation and a high redox potential play an important role in the energy metabolism of these cells. © 2014 Society of Photo-Optical Instrumentation Engineers (SPIE) [DOI: [10.1117/1.JBO.19.9.096005](https://doi.org/10.1117/1.JBO.19.9.096005)]

Keywords: autofluorescence; nicotinamide-adenine-dinucleotide; redox-ratio; cell metabolism; 2p microscopy; spectrally resolved fluorescence lifetime imaging; hybrid detector.

Paper 140346R received Jul. 11, 2014; revised manuscript received Aug. 13, 2014; accepted for publication Aug. 13, 2014; published online Sep. 9, 2014.

## 1 Introduction

Cell metabolism is defined as the sum of the chemical reactions taking place within each cell of a living organism and providing energy for vital processes. A common property of invasive cancers is altered glucose metabolism. Glycolysis first requires the conversion of glucose to pyruvate and further to lactic acid in the cytoplasm of the cell (Fig. 1). This fermentation process occurs in the absence of oxygen. In the presence of oxygen, pyruvate is involved in the citric acid cycle within the mitochondria, which results in the production of the metabolic coenzymes nicotinamide adenine dinucleotide (NADH) and flavine adenine dinucleotide (FAD). As ubiquitous electron carriers they play an important role in oxidative phosphorylation (OXPHOS, see Fig. 1).

In most mammalian cells, OXPHOS plays a central role in energy supply. However, even in the presence of oxygen a metabolic switch to aerobic glycolysis (Warburg effect<sup>1,2</sup>) is often observed for invasive cancers. Warburg's initial observation focused interest on tumor metabolism, mainly because of the widespread clinical application of the imaging technique positron-emission tomography (PET). This technique detects significantly increased glucose uptake in most primary and metastatic human cancers.<sup>3</sup> Although the spatial resolution of PET is low, new techniques have been developed to increase the resolution and, thus, the specificity and sensitivity. One technique, the observation of cell metabolism through time-resolved autofluorescence imaging, is a new and challenging procedure

[for comprehensive reviews on fluorescence lifetime imaging (FLIM) see Ref. 4]. It is based on the detection of the fluorescence lifetime of the metabolic coenzymes and changes of the redox ratio which could be defined as the ratio of the fluorescence intensity of FAD and NADH.<sup>5</sup> A change in the redox ratio is correlated with a change in the fluorescence lifetimes of NADH and FAD.<sup>6</sup>

NADH is located in the mitochondria of living cells as well as the cytoplasm and the cell nucleus. NADH not bound to proteins ("free" NADH) typically possesses a short fluorescence lifetime around 500 ps because of quenching of the reduced nicotinamide by the adenine group. If it is bound to proteins, the lifetime is much longer (around 2.5 ns).<sup>7,8</sup> However, due to the conformational heterogeneity of the different enzymes, bound NADH can have complex lifetime distributions with more than one exponential component.<sup>9</sup> The maximum emission of free NADH is around 470 nm, whereas the maximum is blue-shifted toward 440 nm when it is bound to proteins.<sup>10-13</sup> NADH found in the cell nucleus plays a role in gene expression, but not in metabolic activity.<sup>14-16</sup>

In the literature is described the correlation between metabolic activity, redox ratio and fluorescence lifetime during stem cell differentiation, neurodegenerative diseases, and carcinogenesis. Two-photon autofluorescence studies revealed that during adipogenic differentiation of human salivary gland stem cells the mean fluorescence lifetime of NADH and FAD was longer for differentiated cells than for the nondifferentiated.<sup>17</sup> This was correlated with an increase of oxygen consumption and an increase of aerobic cell metabolism. In a

\*Address all corresponding to: Angelika Rück, E-mail: [angelika.rueck@uni-ulm.de](mailto:angelika.rueck@uni-ulm.de)

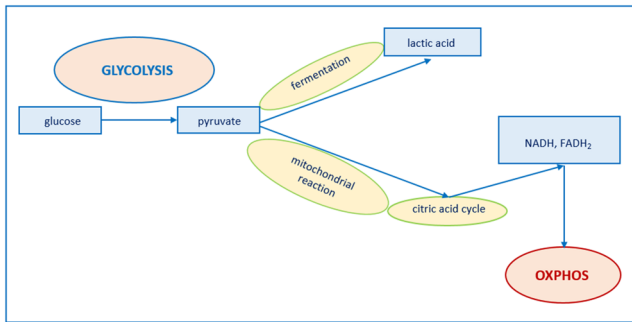


Fig. 1 Glucose metabolism in mammalian cells.

*Caenorhabditis elegans* germ line, different metabolic states of stem cells could be distinguished with the phasor approach to fluorescence lifetime imaging.<sup>9</sup> Metabolic mapping with FLIM showed that during differentiation the concentration of FAD decreases, but the concentration of bound NADH increases with respect to free NADH, correlating with a longer lifetime. NADH lifetime imaging using two-photon microscopy in cerebral tissue *in vivo* showed multiple decaying exponentials, representing different enzyme-bound formulations.<sup>18</sup> The metabolic activity of neurons, astrocytes, vascular endothelial cells, and others were monitored during periods of anoxia.

During carcinogenesis, a shortening of the lifetime of NADH was reported for low grade and high grade precancerous tissue compared with normal tissue, whereas the lifetime of FAD exhibited an elongation.<sup>19</sup> This was correlated with a shift from OXPHOS to glycolysis and neoplastic metabolism. Similarly, metabolic mapping of human breast cells was achieved via multiphoton FLIM of NADH.<sup>20</sup> In another report by Stringari et al.,<sup>21</sup> the metabolic state of intestinal stem cells in a living small intestine was characterized by a high ratio of free/bound NADH and a short lifetime of NADH, indicating glycolysis, as is mostly expected in highly proliferative stem cells and cancer cells.

Due to the discussion above, it is evident that the observation of cell metabolism by autofluorescence FLIM could be a straightforward tool to enhance specificity in fluorescence-guided tumor diagnosis. The method is even considered for use in the clinic for imaging of brain tumors.<sup>22,23</sup> For this indication, the lifetime of NADH was found to be longer in the tumor than in the normal tissue.<sup>22-24</sup> A shortening of NADH lifetime correlated with higher free NADH concentration and glycolytic switch is therefore not an exclusive rule for tumors and depends on the individual situation.

Within this work, we investigated two-photon spectrally resolved FLIM to measure metabolic phenotypes of malignant and nonmalignant oral mucosa cells. In detail, the redox states of the human oral squamous carcinoma cells SCC-25 and SCC-4 as well as the nonmalignant control cell OKF6/TERT-2 were studied. So far, different attempts have been described in the literature to detect the redox state of cells, as optical metabolic imaging (OMI), where the mean lifetimes of NADH and FAD and the fluorescence intensities of both compounds are taken into account.<sup>25</sup> Our focus within this work was NADH imaging, where we tried to discriminate free/bound NADH by spectrally resolved FLIM [SLIM (Refs. 26–28)]. For this, we used a series of narrow band pass filters in combination with a novel hybrid PMT which possess a high detection efficiency and minimal after pulsing.<sup>18</sup> We performed a two-exponential fitting procedure to calculate free/bound NADH ratios within three

different spectral regions, namely  $436 \pm 10$ ,  $470 \pm 10$ , and  $490 \pm 10$  nm. Moreover, different metabolic states could be distinguished with the phasor approach.

## 2 Methodology

### 2.1 Imaging System

In order to investigate multispectral FLIM of autofluorescent molecules, a tunable Ti:Saphir laser (Mai Tai AX HPDS, Spectra Physics, Santa Clara, California) was coupled to a laser scanning microscope (LSM710, Carl Zeiss, Jena, Germany). The Mai Tai laser is a mode-locked 80 MHz “high performance” DeepSee laser with a tuning range of 690 to 1040 nm, a maximum optical output power of about 2.8 W at 800 nm and a pulse width below 100 fs. For autofluorescence imaging, cells were excited with two photons at 720 nm. The average power at the input of the microscope was reduced and measured at the output of the objective lens to be 25 mW. A beam dwell time per pixel of  $1.27 \mu\text{s}$ , which corresponds to a scanning time of 782 ms, has been chosen. Typically, the acquisition time was in the range of several seconds. Taking into account the very short dwell time, which could be achieved due to the use of the newest generation of hybrid detectors (see Fig. 2), the overall irradiation was less than or in the same order of magnitude as in comparable investigations. Moreover, mitochondrial staining with rhodamine 123 after scanning proved that our scanning conditions were not toxic to the cells (data not shown). Spectral detection of FLIM was done using narrow band pass filters at 436 nm (BP  $436 \pm 10$  nm), 470 nm (BP  $470 \pm 10$  nm), and 490 nm (BP  $490 \pm 10$  nm) from AHF Analysentechnik (Tübingen, Germany) and a two channel time-correlated single photon counting (TCSPC) system (Becker & Hickl GmbH, Berlin, Germany) consisting of a Simple-Tau-152-DX, SPC-Image, and the hybrid detector HPM-100-40. This system was coupled to the nondescanned detector (NDD) port of the LSM 710 (see Fig. 2).

For each photon, the TCSPC module determines the location within the scanning area and the time of the photon within the laser pulse period. These parameters were used to build up a two-dimensional photon distribution over the scan area and the time in the fluorescence decay. For the results presented below, we used a high resolution image size of  $256 \times 256$  pixels and 256 time channels. The microscope

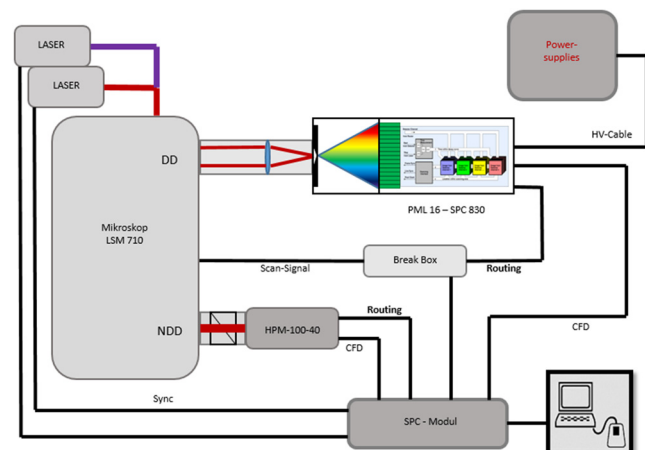


Fig. 2 Multiphoton and single photon fluorescence lifetime imaging/ spectrally resolved fluorescence lifetime imaging (FLIM/SLIM) at the laser scanning microscope (LSM) 710.

objective lens was a 20× magnification NA 0.8 lens (“Plan-Apochromat” 20 × /0.8, Carl Zeiss, Germany). With a zoom factor of 2, an area of 212 × 212 μm<sup>2</sup> was imaged.

## 2.2 Cell Culture Studies

The TERT-immortalized human oral keratinocyte line OKF6/TERT-2<sup>29,30</sup> and two different human oral squamous carcinoma cells (SCC-25, ATCC-Nr. CRL-1628 and SCC-4, ATCC-Nr. CRL-1624) were grown in Dulbecco's Modified Eagle's Medium (DMEM) [Invitrogen (Gibco), Karlsruhe, Germany] in the case of SCC cells and in keratinocyte serum-free medium (SFM) [Invitrogen (Gibco), Karlsruhe, Germany] in the case of OKF6, both supplemented with 10% fetal bovine serum at 37°C and 5% CO<sub>2</sub>. SCC-25 and SCC-4 differed in their expression of fatty acid synthase (FAS),<sup>31</sup> which is overexpressed in several human epithelial cancers. FAS expression in SCC-4 is lower than that in SCC-25, and the epidermal growth factor expression is stronger in SCC-25 than in SCC-4. As discussed in Ref. 31, chemotherapy using FAS as potential target could be more effective for SCC-25. OKF6/TERT-2 cells were used as a nonmalignant, however immortalized control cell line. OKF6/TERT-2 cells yet retained normal growth and differentiation and showed normal phenotype.

For microscopy, all cells were seeded on glass bottom micro-well dishes with a coverglass of 0.16 to 0.19 mm (MatTek, Ashland, Massachusetts) at a density of 150 cells/mm<sup>2</sup> and were allowed to grow for 48 h. Microscopic observation was immediately performed after removing the incubation medium and rinsing twice with indicator free and fetal bovine serum (FCS) free medium at 37°C. All three cell types were imaged under identical experimental conditions (same laser power, objective lens, zoom factor, temperature, time schedule, etc.), which were essential for statistical comparison of the recorded data. To confirm cell viability after scanning, the cells were stained with 1-μM rhodamine-123 (Sigma-Aldrich, St. Louis, Missouri). Intact mitochondria could be demonstrated in cells, which were irradiated with the Ti:Saphir laser under the described experimental conditions (data not shown).

## 2.3 Data Analysis

The analysis of FLIM data was done with SPCImage software (Becker & Hickl GmbH). We performed a 3 × 3 spatial pixel binning (binning factor 1) to obtain decay profiles with ~5000 photons in total. This is assumed to be the approximate minimum number of photons required to perform multiple-component lifetime fits.<sup>18</sup> A two-exponential fitting procedure with  $I(t) = a_1 e^{-t/\tau_1} + a_2 e^{-t/\tau_2}$ , where  $I(t)$  is the fluorescence intensity at time  $t$ ,  $\tau_1$  and  $\tau_2$  are the lifetimes of the first and second fluorescence component, and  $a_1$  and  $a_2$  are their relative contributions was used. The goodness of fit, the  $\chi^2$  value, was  $\leq 1.2 \pm 0.1$  (single-sigma standard deviation). In a first approximation, the first (short) component can be attributed to free NADH, and the second (long) component to protein-bound NADH.<sup>19,20</sup> The widths of the intervals  $\Delta\tau_m$ ,  $\Delta\tau_1$ , and  $\Delta\tau_2$  containing 66% of the corresponding values were also calculated with SPCImage software. The mean lifetime  $\tau_{\text{mean}}$  was calculated to be  $(a_1 \times \tau_1 + a_2 \times \tau_2)/(a_1 + a_2)$ . We also calculated the intensity ratio  $I(\tau_1)/I(\tau_2)$ , which is equal to  $a_1 \tau_1/a_2 \tau_2$ . The total fluorescence intensity per pixel was calculated by summing individual photon counts with MATLAB software. The calculations were done with a binning factor of 1 for a region

of interest and were divided by the pixel number. Alternatively to the two-exponential fitting procedure, different decaying states were confirmed using global analysis program SimFCS 3.0.<sup>32</sup> This approach leads to faster solutions and might be important for various applications.

## 2.4 Statistics

For statistical evaluation, four different samples were used for every spectral channel (436, 470, and 490 nm, respectively) for every cell type. In total, 150 single images were measured in the case of OKF6/TERT-2, 144 single images in the case of SCC25 and 163 images of SCC4 cells. For statistical calculations SigmaPlot 11.0 (Systat Software Inc., San Jose, California) was used. Statistical differences between different groups were analyzed with Kruskal-Wallis one-way analysis of variance on ranks followed by a pairwise multiple comparison procedure. The differences in the mean values among the treatment groups were taken as significant when they were greater than would be expected by chance; the difference is statistically significant when  $P \leq 0.001$ . When the normality test (Shapiro-Wilk) showed a normal distribution of the data, the Holm-Sidak method was used as a pairwise multiple comparison procedure. When the normality test or the equal variance test failed, the Dunn's method was used.

## 3 Results

### 3.1 FLIM within Spectrally Different Emission Channels

As discussed in Sec. 1, the fluorescence spectra of free and protein bound NADH possess maxima at 470 and 440 nm, respectively, when excited between 340 and 360 nm.

Therefore, FLIM was performed around  $436 \pm 10$  nm,  $470 \pm 10$  nm, and  $490 \pm 10$  nm using narrow band-pass filters (BP) of the same optical density. The spectral range from 470 to 500 nm is related to the emission maximum of free NADH. The reason for the additional use of  $490 \pm 10$  nm was to determine whether or not the separation of free and protein bound NADH is improved when the spectral gap between them is increased. Two-photon excitation was done in all cases at 720 nm. Since the emission spectra of free and bound NADH are highly overlapping, the lifetimes within every channel represent both components with different relative contributions. A two-exponential fitting procedure was used to calculate the fluorescence lifetimes of bound and unbound NADH.

The first (short) fit component was correlated to free NADH, whereas the second (long) component contributed more to protein bound NADH. FLIM was studied in OKF6/TERT-2, SCC-4, and SCC-25 cells. The OKF6/TERT-2 cell served as control (see Sec. 2.2). FLIM of the mean lifetime  $\tau_{\text{mean}}$  and the distribution histogram for the two spectral regions 436 and 470 is shown in Fig. 3 for all cells investigated. The lifetime is represented in false colors. Unbound NADH should be found in a higher amount around 470 nm. In fact, the mean lifetime in the spectral region of 470 nm shifts to shorter values compared to that of 436 nm for all cells. A higher contribution of the short lifetime component within 470 nm was also confirmed with the phasor approach [see Figs. 4(a) and 4(b) for SCC-4 cells]. A further shortening, although statistically not significant, could be observed for 490 nm (see Fig. 5). This means that the contribution of

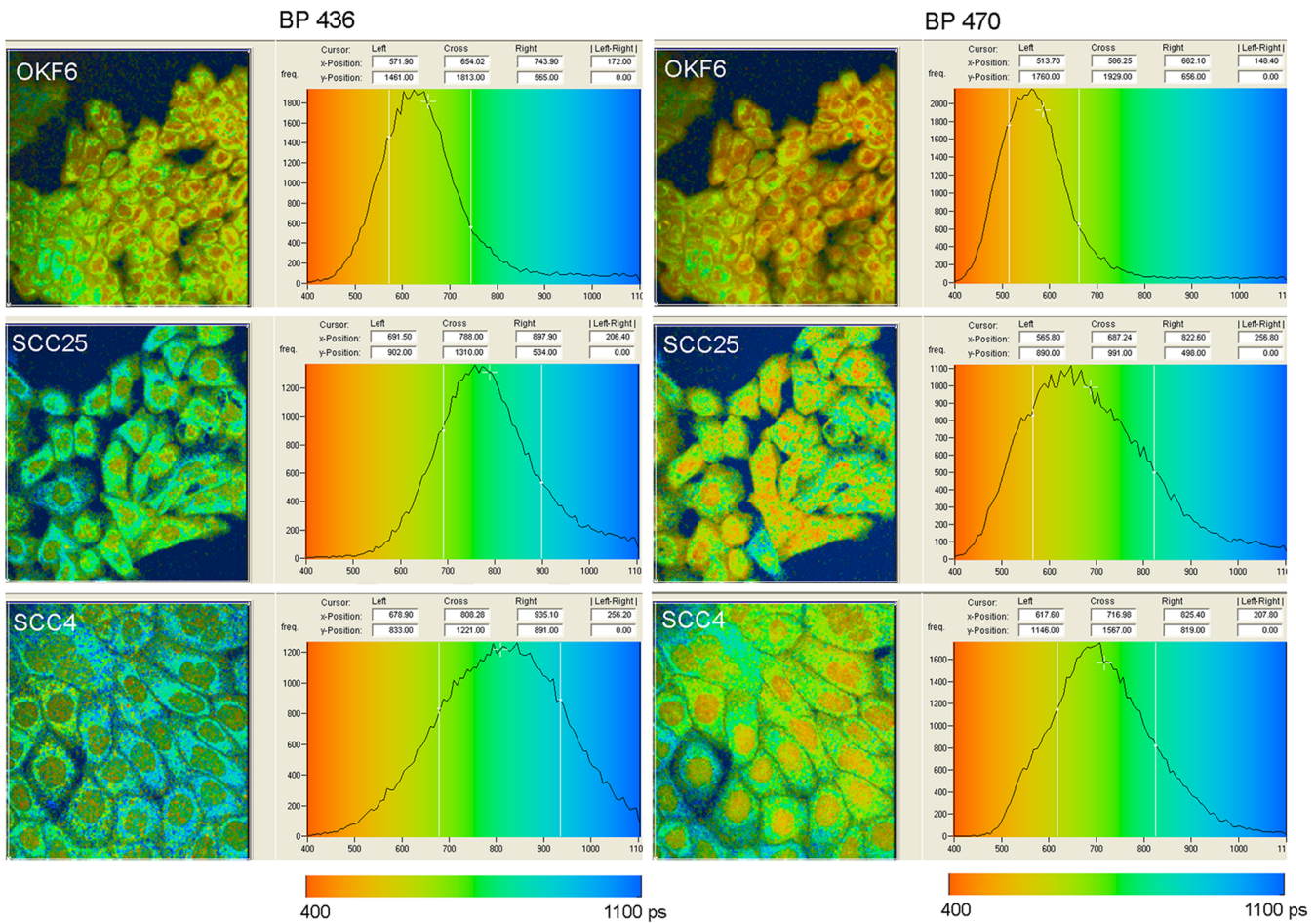


**Fig. 3** FLIM and distribution histogram of the mean lifetime of NADH of OKF6/TERT-2, SCC-25, and SCC-4 cells within two emission channels BP 436 ( $436 \pm 10$  nm) and BP 470 ( $470 \pm 10$  nm). The histograms show the distribution of the  $\tau_m$ -value within the range 400 to 1100 ps.

bound NADH decreases from 470 to 490 nm, which could improve the spectral separation between free and bound NADH. A minor contribution of FAD fluorescence to the spectral region around 490 nm cannot be excluded.

As demonstrated in the box plot in Fig. 5, the difference in the mean lifetime proven to be statistically significant in most cases using the Kruskal-Wallis one way analysis of variance on ranks, followed by a pairwise multiple comparison procedure (Holm-Sidak method). Not significant was the difference between 470 and 490 nm, especially for the SCC-4 cells. The shift to shorter lifetimes correlates well with the decrease of the amplitude  $a_2$  of the long component. The contribution of bound NADH was, in general, less than that of unbound NADH and decreased by approximately 2% to 2.5% at 470 nm compared with 436 nm then further decreased by 0.5% to 1% at 490 nm due to a decreased influence of bound NADH. Although the fluorescence quantum yield of bound NADH is four times higher than of unbound NADH, the fluorescence intensity was highest for all cell types at 470 nm, as demonstrated in Fig. 6. The differences for the different channels were statistically significant ( $P \leq 0.001$ ) with the Kruskal-Wallis one way analysis of variance on the ranks. Since optical density of all three filters was proven to be the same (data not shown), the intensity difference confirms the higher contribution of unbound NADH to the total fluorescence intensity.

### 3.2 FLIM of Different Cell Lines

The fluorescence intensities of OKF6/TERT-2, SCC-25, and SCC-4 cells, which were calculated as total photon counts during imaging within an area of  $3 \times 3$  pixels (binning 1), are demonstrated in Fig. 6. The intensity was always lower for both SCC cell lines compared with OKF6/TERT-2. The reduced fluorescence intensity could indicate a decrease in the total amount of NADH. This is in contrast to a variety of cancers, including breast cancer,<sup>33,34</sup> whereas it was similar for squamous carcinoma as well as oral and cervical dysplasia.<sup>35–37</sup> Whether this is due to a change in the ratio of free/bound NADH was proved further by inspecting the fluorescence lifetimes. As demonstrated in Fig. 3, the value for  $\tau_m$  was increased from the nonmalignant OKF6/TERT-2 to malignant SCC-25 and SCC-4 cells, respectively, which was statistically significant for all spectral channels ( $P \leq 0.001$ ), as proven by Kruskal-Wallis one way analysis followed by a pairwise multiple comparison procedure (Holm-Sidak method, see Fig. 5). The phasor approach confirmed an increase of longer decaying components for malignant versus nonmalignant cells [see Figs. 4(c) and 4(d)]. An elongation was observed for  $\tau_1$  which was statistically significant ( $P \leq 0.001$ , Dunn's method), whereas a slight decrease for  $\tau_2$  was observed for SCC-4 compared with SCC-25. The decrease, however, was not statistically significant. As shown in Fig. 5, SCC-4 cells exhibited the longest  $\tau_1$ , whereas OKF6/TERT-2 decayed in the shortest way.  $\tau_1$

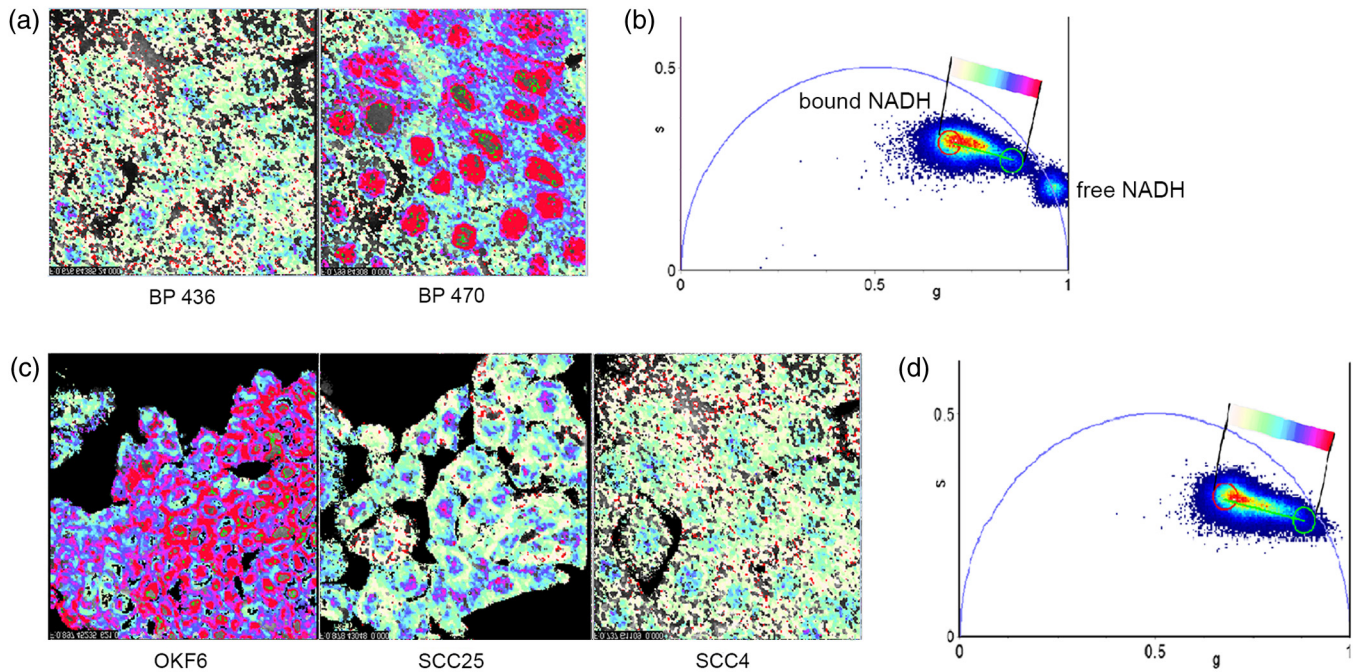


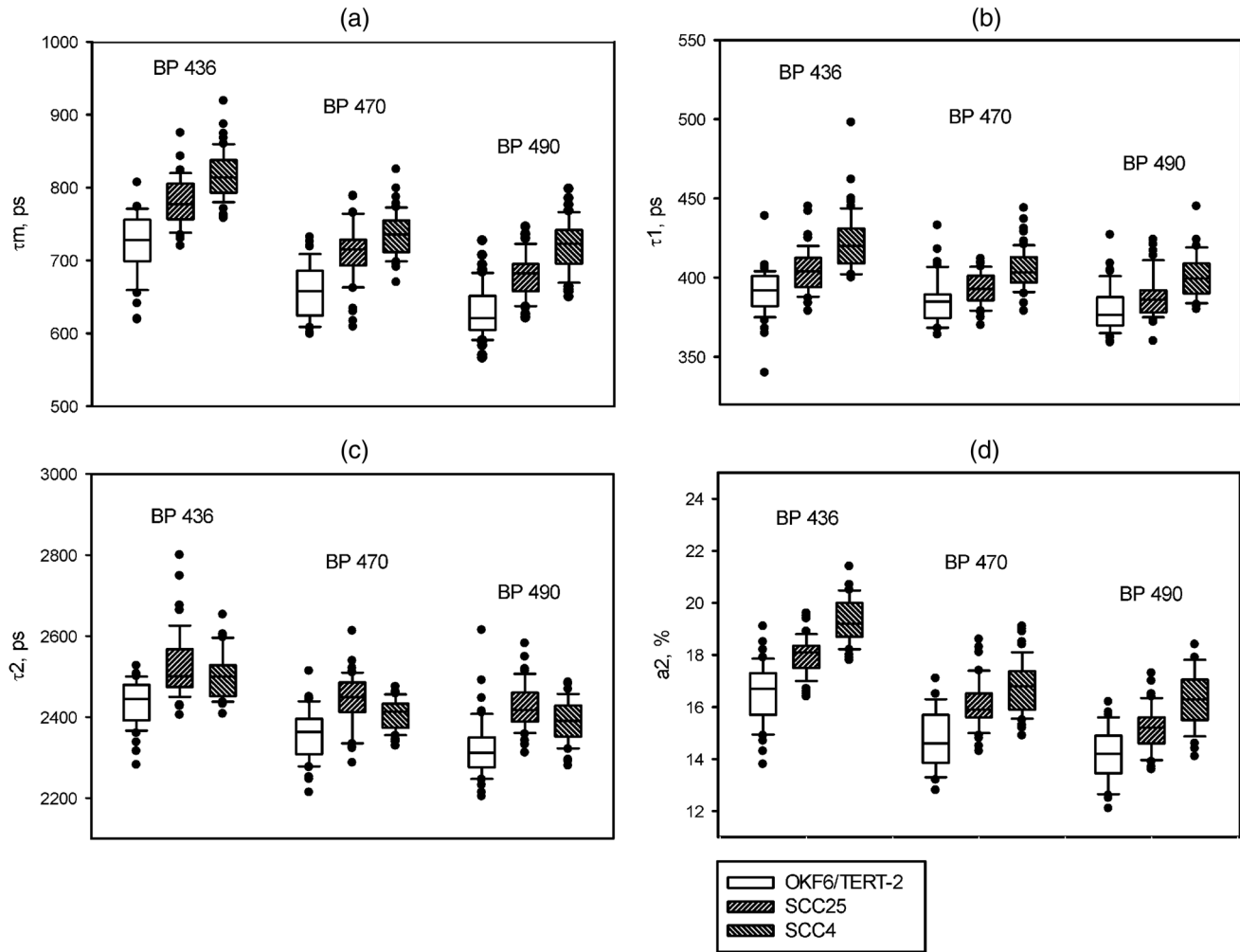
**Fig. 4** (a) NADH maps of FLIM images by the phasor approach of SCC-4 cells within two emission channels BP 436 and BP 470. (b) Phasor plot shows location of free/bound cellular NADH as well as location of free NADH in solution. The NADH maps (c) and phasor plot (d) of FLIM of OKF6/TERT-2, SCC-25, and SCC-4 cells, measured within emission channel BP 436, demonstrate a decrease of free/bound NADH within the cells from nonmalignant OKF6/TERT-2 to malignant SCC-25 and SCC-4. The color scale from red to white indicates the change of the relative concentration of free and bound NADH, from high (red) to low (white) ratios of free/bound NADH.

is correlated with the lifetime of free NADH. A lifetime of  $420 \pm 10$  ps was measured by us for NADH in water (data not shown). The slight difference for the cells could be due to different microenvironments such as pH and viscosity and may reflect changes in dynamic quenching.<sup>38</sup> For  $\tau_2$ , the difference was significant only for the pairs OKF6/TERT-2 versus SCC-4 and SCC-25 (Dunn's method).  $\tau_2$  is correlated with the lifetime of bound NADH. The longer values for SCC-4 and SCC-25 could be due to a different protein binding compared with OKF6/TERT-2. Whether the slight difference between SCC-4 and SCC-25 is due to different metabolic activities has to be proven further. A different ability to express metabolic oncogenes has been reported.<sup>31</sup> In addition, SCC-4 showed a strong tendency to form large progressively growing colonies, which could be related to their high tumorigenic behavior.<sup>30</sup>

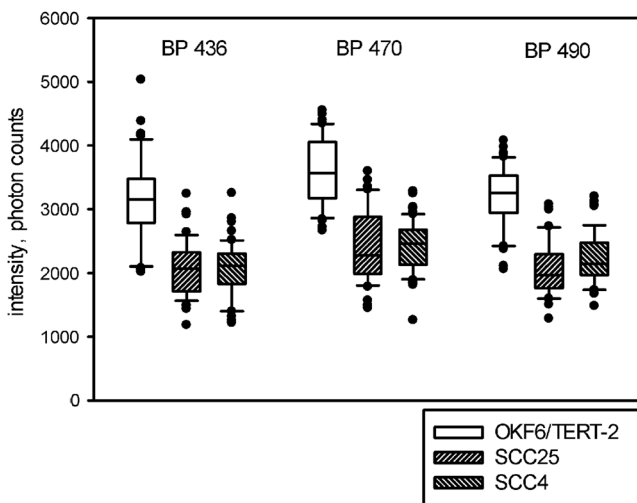
Although the lifetime is a critical parameter for the definition of the microenvironment, for characterization of different cell types the relative contribution of free/bound components probably plays a more essential role. A change in the metabolic activity could not only provide a change in the fluorescence lifetime of both free and bound NADH, but also a change in their relative contributions.<sup>20,39</sup> As shown in Fig. 5, SCC-4 cells exhibited the highest contribution of bound NADH. The differences in  $a_2$  were proven to be statistically significant ( $P \leq 0.001$ , Dunn's method for BP 436 and BP 470 and Holm-Sidak method for BP 490) for all cells. The larger amplitude  $a_2$  is also responsible for the longer lifetime  $\tau_m$  in the case of SCC-4 cells. Reduced fluorescence intensity as demonstrated in Fig. 6 for SCC cells is, therefore, not due to reduced bound NADH, but possibly to a reduced amount of total NADH.

Figure 7 represents (in false colors) the relative intensity of the short compound versus the long compound  $I(\tau_1)/I(\tau_2)$ , which is equal to  $a_1\tau_1/a_2\tau_2$ . For SCC-4, the long lifetime compound is prominent and the concentration is high in the cytoplasm and seems to be correlated with mitochondria (see orange color at BP 436 in Fig. 7). In the case of nonmalignant OKF6/TERT-2, a short compound which is significantly localized in the cell nucleus, is observed in a high concentration (blue color in Fig. 7 at BP 470). This fact is interesting because free NADH in the cell nucleus is known to play a role in the regulation of gene expression and is enhanced in cells where growth is stimulated.<sup>14</sup> The box plot in Fig. 8 demonstrates that the mean ratio  $I_{\text{short}}/I_{\text{long}}$  shows a significant difference ( $P \leq 0.001$ , Dunn's method) for all cells at 436 and 490 nm. At 470 nm, the difference is significant only for OKF6/TERT-2 versus SCC-25 and SCC-4 cells. The contribution of the different decaying components for the cells investigated was also confirmed with the phasor approach [see Figs. 4(c) and 4(d)].

In Fig. 9, the box plot of the width of the interval including 66% of the lifetime values is demonstrated.  $\Delta\tau_m$ ,  $\Delta\tau_1$ , and  $\Delta\tau_2$  were, in most cases, enhanced for SCC-25 and SCC-4 compared with OKF6/TERT-2 for all spectral channels. The differences for  $\Delta\tau_m$  for all three cell lines was statistically proven significant ( $P \leq 0.001$ ) with Kruskal-Wallis one way analysis followed by a pairwise multiple comparison procedure (Dunn's method for BP 436, BP 470, and Holm-Sidak method for BP 490). The smaller intervals in the case of OKF6/TERT-2 could be explained by attributing the better statistics of these cells to higher photon counts (see Fig. 6). Additionally, this also supports the assumption that both cancer cells showed higher diversity and, therefore, various binding states of NADH.



**Fig. 5** Statistical evaluation (box plot) of the lifetime parameters for OKF6/TERT-2, SCC25, and SCC4 measured for the three emission channels BP 436, BP 470, and BP 490, in detail, the mean lifetime  $\tau_m$  (a), the first (short) fluorescence component  $\tau_1$  (b), the second (long) component  $\tau_2$  (c), and  $a_2$ , which is the relative contribution of the protein bound NADH (d).



**Fig. 6** Total fluorescence intensity for OKF6/TERT-2, SCC-25, and SCC-4 at 436, 470, and 490 nm, calculated as total photon counts/pixel with binning 1.

## 4 Discussion

The aim of this work was to evaluate spectrally resolved multi-photon NADH FLIM to investigate cell metabolism in metabolic phenotypes of malignant and nonmalignant oral mucosa cells. A measure for cell metabolism could be the relative contribution of protein bound and free NADH. Our investigation was, therefore, focused on the spectral and temporal separation of bound and free NADH, which was achieved using different narrow band path filters correlating with the fluorescence maxima of bound and free NADH, respectively. Other investigators tried to measure cell metabolism taking into account broad band NADH and FAD.<sup>25</sup> We did a two exponential fitting procedure for the fluorescence intensity decay as well as a phasor plot analysis within the different spectral regions. As expected, a higher contribution of bound NADH could be observed for all cells in the spectral region at 436 nm.

The mean lifetime  $\tau_m$  was increased from the nonmalignant OKF6/TERT-2 to the malignant SCC-25 and SCC-4 cells, which was mainly induced by an increase of the amplitude  $a_2$ . This increase was observed in all spectral channels but mostly at 436 nm, where the contribution of bound NADH is highest, confirming that bound NADH is increased in SCC

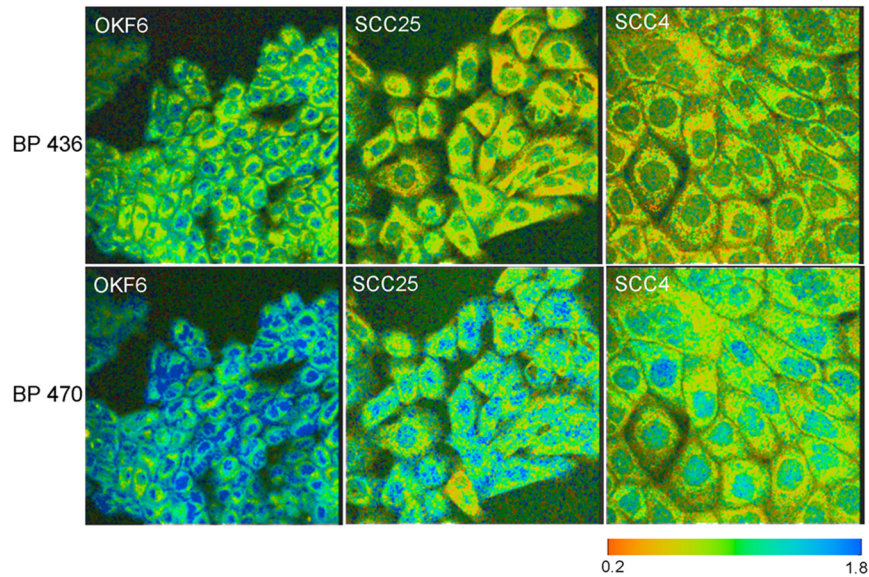


**Fig. 7** Distribution of  $a_1\tau_1/a_2\tau_2$  in false colors for the three cell lines in the two spectral regions BP 436 and 470.

cells. In a recent publication by Walsh et al.,<sup>25</sup> NADH  $\tau_m$  of a variety of malignant breast cancer cells was increased over that of a noncancerous mammary epithelium cell, whereas for other subtypes a decrease was observed. From our fluorescence intensity measurements (Fig. 6), it seems that the total amount of NADH is less for both SCC cells compared with the nonmalignant OKF6/TERT-2, similar to reports in the literature for squamous carcinoma as well as oral and cervical dysplasia.<sup>36,40</sup> From the width of the lifetime intervals (Fig. 9), it could be correlated that SCC cells showed a higher diversity and variation of binding states of NADH than the nonmalignant cell. The ratio of free/bound NADH was decreased from OKF6 to SCC-25 to SCC-4 (see Fig. 8). The decrease from nonmalignant to malignant cells was more pronounced at 470 nm, confirming a lower contribution of free NADH in both SCC cells. This, together with the fact that a high concentration of bound NADH was found in cytoplasmic organelles, mainly mitochondria (see Figs. 4 and 7), indicates that the OXPHOS plays an important role in the cell metabolism of SCC cells. The redox potential

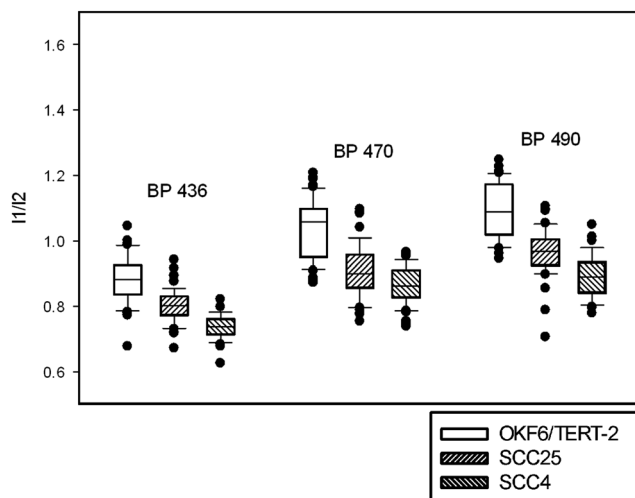


**Fig. 8** Box plot of the ratio of the intensity  $I_{\text{short}}/I_{\text{long}} = I_1/I_2$ .

NAD<sup>+</sup>/NADH is dependent on the cell metabolism and, therefore, on the ratio of free/bound NADH, which could be influenced by therapeutic drugs.<sup>41</sup> It seems that the redox potential is highest for the SCC-4 cells, followed by SCC-25 and OKF6.

As mentioned in Sec. 1, a shortening of the lifetime of NADH, which could indicate aerobic glycolysis, is not an exclusive rule for tumor cells. This was demonstrated in this work and also by others.<sup>22–25</sup> In contrast, the situation is even more complex. Whereas in our case the increase of  $\tau_m$  from nonmalignant to malignant oral mucosa cells was correlated with a decrease of the fluorescence intensity of NADH and a decrease of free/bound NADH,  $\tau_m$  did not correlate with the redox ratio for various malignant and nonmalignant breast cells.<sup>25</sup> In that case, the additional consideration of FAD helped to improve the reliability of OMI.

An alternative explanation for the negative “Warburg effect” found in this work could be oxidative stress due to irradiation with femtosecond laser pulses.<sup>42</sup> Oxidative stress could lead to misleading results due to an increase of bound nicotinamide adenine dinucleotide phosphate (NADPH) fluorescence.<sup>43</sup> However, to avoid this situation, for single-cell populations, we carefully treated and imaged all cell types under exactly the same experimental conditions. Only a systemic effect might be considered.

Observation of cell metabolism by NADH FLIM is a straightforward but not trivial method. In an attempt to improve metabolic imaging, alternative strategies have been developed, such as an introduction of the OMI index<sup>25</sup> or the time-correlated dynamics of a mitochondrial membrane potential reporter fluorescence.<sup>44</sup> Due to the complex variation and conformational heterogeneity of free and bound NADH, global analysis of spectral- and time-resolved data could resolve the system. Different global analysis algorithms have been developed. We published a multiexponential fitting procedure for a 16 channel multianode FLIM system.<sup>45</sup> The phasor representation, also demonstrated in this work, has been described to be very powerful for the analysis of lifetime imaging data (lifetime phasor<sup>46</sup>) and/or spectral imaging data (spectral phasor<sup>47</sup>). Our work showed that the combination of both spectrally and

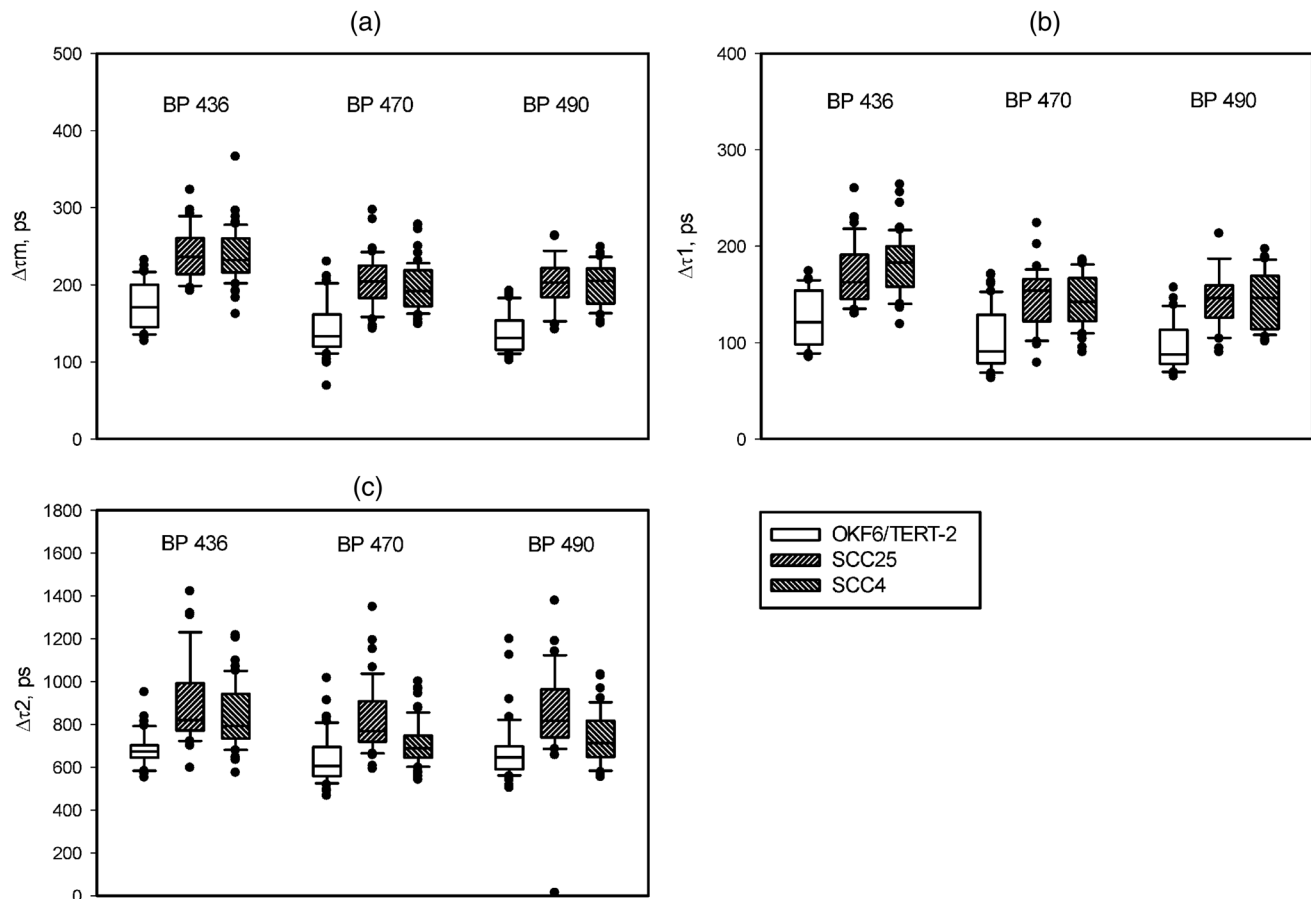


**Fig. 9** Box plot of widths of interval including 66% of all measured lifetime values for OKF6/TERT-2, SCC-25, and SCC-4 measured for the three emission channels BP 436, BP 470, and BP 490:  $\Delta\tau_m$  (a),  $\Delta\tau_1$  (b),  $\Delta\tau_2$  (c).

time-resolved analyses could improve the reliability of NADH FLIM and redox imaging.

The results presented within this work were obtained from cells in culture. Investigations aiming to improve metabolic imaging by FLIM in the clinical situation are even more complex. Before applying the presented method for tissues *in vivo* from biopsies or patients, one has to consider other parameters such as tissue oxygenation, tissue vascularization, or tissue architecture. This requires an effort to combine different imaging techniques, such as optical coherence tomography (OCT), magnetic resonance imaging (MRI), and FLIM.

### Acknowledgments

This work was carried out with financial support by the Ministry of Research and Development of Germany, order FKZ: 13N11179 ("FLENDOS") and 13N12942 ("METAPHOR"). OKF6/TERT-2 was provided by J. Rheinwald and the Cell Culture Core of the Harvard Skin Disease Research Center, Boston, MA.

### References

- R. A. Gatenby and R. J. Gillies, "Why do cancers have high aerobic glycolysis?," *Nat. Rev.* **4**(11), 891–899 (2004).
- O. Warburg, "On the origin of cancer cells," *Science* **123**(3191), 309–314 (1956).
- S. S. Gambhir, "Molecular imaging of cancer with positron emission tomography," *Nat. Rev. Cancer* **2**(9), 683–693 (2002).
- A. Periasamy and R. M. Clegg, *FLIM Microscopy in Biology and Medicine*, A. Periasamy and R. M. Clegg, Eds., Taylor & Francis Group, Boca Raton, FL (2009).
- B. Chance et al., "Oxidation-Reduction ratio studies of mitochondria in freeze-trapped samples," *J. Biol. Chem.* **254**(11), 4764–4771 (1979).
- M. C. Skala et al., "In vivo multiphoton microscopy of NADH and FAD redox states, fluorescence lifetimes, and cellular morphology in precancerous epithelia," *PNAS* **104**(49), 19494–19499 (2007).
- J. R. Lakowicz et al., "Fluorescence lifetime imaging of free and protein-bound NADH," *PNAS* **89**(4), 1271–1275 (1992).
- Y. Wu, W. Zheng, and J. Y. Qu, "Sensing cell metabolism by time-resolved autofluorescence," *Opt. Lett.* **31**(21), 3122–3124 (2006).
- C. Stringari et al., "Phasor approach to fluorescence lifetime microscopy distinguishes different metabolic states of germ cells in a live tissue," *PNAS* **108**(33), 13582–13587 (2011).
- K. König and H. Schneckenburger, "Laser-induced autofluorescence for medical diagnosis," *J. Fluoresc.* **4**(1), 17–40 (1994).
- J. R. Lakowicz, *Principles of Fluorescence Spectroscopy*, 2nd ed., Kluwer/Academic Plenum Publishers, New York (1999).
- R. Huber et al., "Protein binding of NADH on chemical preconditioning," *J. Neurochem.* **75**(1), 329–335 (2000).
- N. L. Vekshin, *Photonics of Biopolymers*, Springer, Berlin (2002).
- D. Li, W. Zheng, and J. Y. Qu, "Time-resolved spectroscopic imaging reveals the fundamentals of cellular NADH fluorescence," *Opt. Lett.* **33**(20), 2365–2367 (2008).
- Q. Zhang, D. W. Piston, and R. H. Goodman, "Regulation of corepressor function by nuclear NADH," *Science* **295**(5561), 1895–1897 (2002).
- C. C. Fjeld, W. T. Birdsong, and R. H. Goodman, "Differential binding of NAD<sup>+</sup> and NADH allows the transcriptional corepressor carboxyl-terminal binding protein to serve as a metabolic sensor," *PNAS*, **100**(16), 9202–9207 (2003).

17. K. König, A. Uchugonova, and E. Gorjup, "Multiphoton fluorescence lifetime imaging of 3D-stem cell spheroids during differentiation," *Microsc. Res. Tech.* **74**(1), 9–17 (2011).
18. M. A. Yaseen et al., "In vivo imaging of cerebral energy metabolism with two-photon fluorescence lifetime microscopy of NADH," *Biomed. Opt. Express* **4**(2), 307–321 (2013).
19. M. C. Skala et al., "In vivo multiphoton fluorescence lifetime imaging of protein-bound and free NADH in normal and pre-cancerous epithelia," *J. Biomed. Opt.* **12**(2), 024014 (2007).
20. D. K. Bird et al., "Metabolic mapping of MCF10A human breast cells via multiphoton fluorescence lifetime imaging of the coenzyme NADH," *Cancer Res.* **65**(19), 8766–8773 (2005).
21. C. Stringari et al., "Metabolic trajectory of cellular differentiation in small intestine by phasor fluorescence lifetime microscopy of NADH," *Sci. Rep.* **2**, 1–9 (2012).
22. Y. Sun et al., "Fluorescence lifetime imaging microscopy for brain tumor image-guided surgery," *J. Biomed. Opt.* **15**(5), 056022 (2010).
23. J. Leppert et al., "Multiphoton excitation of autofluorescence for microscopy of glioma tissue," *Neurosurgery* **58**(4), 759–767 (2006).
24. J. McGinty et al., "Wide-field fluorescence lifetime imaging of cancer," *Biomed. Opt. Express* **1**(2), 627–640 (2010).
25. A. J. Walsh et al., "Optical metabolic imaging identifies glycolytic levels, subtypes, and early-treatment response in breast cancer," *Cancer Res.* **73**(20), 6164–6174 (2013).
26. A. Rück et al., "SLIM: a new method for molecular imaging," *Micro Res. Technol.* **70**(5), 485–492 (2007).
27. C. Biskup et al., "Spectrally resolved fluorescence lifetime imaging microscopy: SLIM/mwFLIM," in *FLIM Microscopy in Biology and Medicine*, A. Periasami and R. M. Clegg, Eds., pp. 211–244, Taylor & Francis Group, Boca Raton, FL (2009).
28. W. Becker, A. Bergmann, and C. Biskup, "Multispectral fluorescence lifetime imaging by TCSPC," *Microsc. Res. Tech.* **70**(5), 403–409 (2007).
29. M. A. Dickinson et al., "Human keratinocytes that express hTERT and also bypass a p16(INK4a)-enforced mechanism that limits life span become immortal yet retain normal growth and differentiation characteristics," *Mol. Cell Biol.* **20**(4), 1436–1447 (2000).
30. J. G. Rheinwald and M. A. Beckett, "Tumorigenic keratinocyte lines requiring anchorage and fibroblast support cultures from human squamous cell carcinomas," *Cancer Res.* **41**(5), 1657–1663 (1981).
31. M. Agostini et al., "Fatty acid synthase is required for the proliferation of human oral squamous carcinoma cells," *Oral Oncol.* **40**(7), 728–735 (2004).
32. E. Gratton, "Globals Software SimFCS 3.0," Laboratory for Fluorescence Dynamics, University of California, Irvine, <http://www.lfd.uci.edu/globals/> (2006–2014).
33. J. H. Ostrander et al., "Optical redox ratio differentiates breast cancer cell lines based on estrogen receptor status," *Cancer Res.* **70**(11), 4759–4766 (2010).
34. A. Walsh et al., "Optical imaging of metabolism in HER2 overexpressing breast cancer cells," *Biomed. Opt. Express* **3**(1), 75–85 (2012).
35. M. C. Skala et al., "Multiphoton microscopy of endogenous fluorescence differentiates normal, precancerous, and cancerous squamous epithelial tissues," *Cancer Res.* **65**(4), 1180–1186 (2005).
36. K. Edward et al., "In vivo layer-resolved characterization of oral dysplasia via nonlinear optical micro-spectroscopy," *Biomed. Opt. Express* **3**(7), 1579–1593 (2012).
37. N. Ramanujam et al., "In vivo diagnosis of cervical intraepithelial neoplasia using 337-nm-excited laser-induced fluorescence," *Proc. Natl. Acad. Sci. U. S. A.* **91**(21), 10193–10197 (1994).
38. J. Lakowicz, *Principles of Fluorescence Spectroscopy*, Plenum Publishers, New York (1999).
39. H. W. Guo et al., "Reduced nicotinamide adenine dinucleotide fluorescence lifetime separates human mesenchymal stem cells from differentiated progenies," *J. Biomed. Opt.* **13**(5), 050505 (2008).
40. A. Uppal and P. K. Gupta, "Measurement of NADH concentration in normal and malignant human tissues from breast and oral cavity," *Biotechnol. Appl. Biochem.* **37**(1), 45–50 (2003).
41. A. Chorvatova et al., "Effect of ouabain on metabolic oxidative state in living cardiomyocytes evaluated by time-resolved spectroscopy of endogenous NAD(P)H fluorescence," *J. Biomed. Opt.* **17**(10), 101505 (2012).
42. K. König et al., "Two-photon excited lifetime imaging of autofluorescence in cells during UVA and NIR photostress," *J. Microsc.* **183**(Pt 3), 197–204 (1996).
43. A. Chorvatova et al., "Time-resolved fluorescence spectroscopy investigation of the effect of 4-hydroxynonenal on endogenous NAD(P)H in living cardiac myocytes," *J. Biomed. Opt.* **18**(6), 067009 (2013).
44. V. K. Ramanujan, "Metabolic imaging in multiple time scales," *Methods* **66**(2), 222–229 (2014).
45. D. Strat et al., "Spectrally resolved fluorescence lifetime imaging: FRET Global Analysis with a one- and two-exponential donor model," *J. Biomed. Opt.* **16**(2), 026002 (2011).
46. M. A. Digman et al., "The phasor approach to fluorescence lifetime imaging analysis," *Biophys. J.* **94**(2), 14–16 (2008).
47. F. Fereidouni, A. N. Bader, and H. C. Gerritsen, "Spectral phasor analysis allows rapid and reliable unmixing of fluorescence microscopy spectral images," *Opt. Express* **20**(12), 12729–12741 (2012).

**Angelika Rück** studied chemistry at the University of Ulm. She holds the position of the leader of the core facility laser microscopy of the medical faculty at the University Ulm and is responsible for microscopic applications in the field of biomedical research. Her specialties are developments of methods for FLIM, SLIM, and PLIM, for detection and dynamic analysis of signal transduction pathways in living cells, cell metabolism, tumor biology, and neurodegenerative diseases.

**Sviatlana Kalinina** is a biophysicist with a background in both physics and cell physiology. She got her diploma at Belarusian State University (Belarus) and her PhD at Karlsruhe Institute of Technology (Germany). She currently works as a scientist at University of Ulm (Germany) within a microscopy research group focused on fluorescence lifetime imaging for the investigation of cellular metabolism.

Biographies of the other authors are not available.